

Plasmon Mode Engineering with Electrons on Helium

C.A. Mikolas,^{1,*} N.R. Beysengulov,^{1,2} A.J. Schleusner,¹ D.G. Rees,² C. Undershute,¹ and J. Pollanen^{1,†}

¹*Department of Physics & Astronomy, Michigan State University, East Lansing, MI 48824, USA*

²*EeroQ Corporation, Chicago, IL 60651, USA*

(Dated: August 22, 2024)

An ensemble of electrons trapped above the surface of superfluid helium is a paradigm system for investigating, and controlling, the collective charge dynamics of low-dimensional electronic matter. Of particular interest is the ability to engineer the spatial and spectral structure of surface plasmon modes in this system for integration into hybrid quantum systems or circuit quantum electrodynamic device architectures. Here we present experiments on a hybrid electron-on-helium microchannel device designed to host microwave-frequency plasmon modes having a spatial structure dictated by the geometry of the microchannel confinement. The plasma oscillations are generated via local microwave frequency excitation of the electrons in the microchannel. When this excitation is resonant with a particular surface plasmon-mode it produces a non-equilibrium decrease in the electron conductance, which we detect via simultaneous transport measurements. We find that the spatial structure of the surface plasmons is in excellent agreement with our device design parameters and modeling, and their frequency can be tuned over a broad range (several GHz) by precisely varying the areal density of electrons in the channel. By measuring the plasma resonance spectrum lineshape, and its power dependence, we can quantify the level of spatial homogeneity associated with each plasmon mode. The results highlight the versatility of electrons on helium as a model system for investigating, and engineering, the collective mode structure of low-dimensional Coulomb liquid and solid states and demonstrate a viable path for integrating precisely engineered surface plasmons in electrons on helium with future hybrid circuit quantum electrodynamic systems.

I. INTRODUCTION

Circuit quantum electrodynamics (cQED) [1, 2] and the toolkit of microwave frequency optomechanics [3] have enabled the development of sophisticated quantum control and measurement protocols for a wide variety of quantum systems ranging from superconducting circuits [4] and semiconductor spins [5], to systems of trapped electrons [6–8], as well as nano- and micromechanical oscillators [9–12]. These techniques can also be leveraged as powerful experimental tools for investigating microwave frequency *collective* phenomena in quantum systems composed of many interacting particles or degrees of freedom [13]. For example, when coupled with superconducting circuits, these approaches have been used to study collective modes in magnonic [14–19] and phononic [20–25] systems and to investigate the dynamics of spin ensembles [26, 27].

Electrons trapped above the surface of condensed noble gas substrates, such as superfluid helium or solid neon, are emerging as promising systems for integration with cQED architectures and microwave frequency devices for quantum information processing [28–32]. At the level of single electrons, cQED techniques have been used to investigate the in-plane orbital states of electrons on helium [6, 33] and have recently been utilized to realize high-coherence charge qubits on the surface of solidified neon [7, 8]. In contrast to single electron dynamics, these systems can also host a wide variety of collective

charge modes including plasmonic [34, 35] and magneto-plasmonic excitations [36–40], as well as hybrid modes coupling the dynamics of multiple degrees of freedom [41–43]. Additionally, ensembles of electrons on helium have been strongly coupled to three-dimensional microwave cavities to study cyclotron resonance [44, 45] and integrated into hybrid circuits in which an electron ensemble is placed above a planar microwave resonator [46].

Fully leveraging cQED-type techniques to study the high-frequency dynamics of electrons on helium requires the development of devices that have not only an optimized microwave environment [46], but also the ability to engineer and manipulate the collective modes of the electron system via precise spatial control. In this work, we address the latter of these aspects by realizing a device that enables precision control over the spatial distribution of electrons in a microchannel geometry, providing the ability to engineer, excite, and detect plasmonic excitations with frequencies in a range compatible with cQED-based systems. Local microwave excitation resonantly couples to the plasmon modes, which we detect via changes in the electron conductance determined by simultaneous transport measurements. By precisely varying the electron density in the microchannel, we can tune the frequency of the modes by several GHz. Analyzing the power dependent plasmon mode lineshape allows us to infer the level of spatial homogeneity of electrons in the microchannel, which we compare with simulations of the electron density. Finally, we highlight how this type of device and our results demonstrate the overall system control necessary to integrate with future low-loss microwave cQED architectures.

* mikolasc@msu.edu

† pollanen@msu.edu

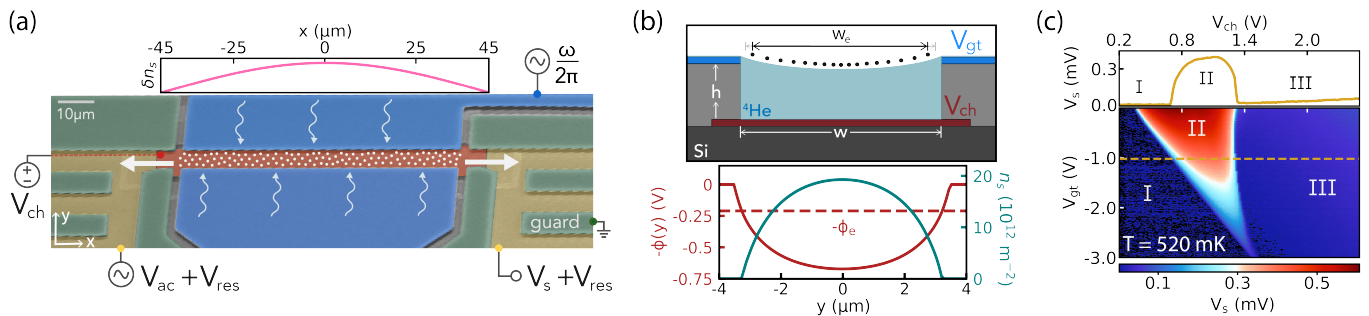


FIG. 1. (a) False color scanning electron micrograph of the microchannel device. Grounded guard electrodes (green) patterned above a resist layer surround reservoir electrodes (yellow) located beneath. The central microchannel region between the two reservoirs consists of a channel electrode (red) and top side gate electrode (blue). An ac drive voltage V_{ac} at frequency f_{ac} drives the electrons (white dots) through the channel and the resulting transport signal V_s is detected via a lock-in amplifier. A $\omega/2\pi$ frequency microwave signal on the gate electrode generates longitudinal plasmons (shown schematically in the δn_s plot). (b) Top panel: Schematic cross section view across $x = 0$ of the channel with a fixed dc bias voltage (i.e. no microwave drive) on the side gate electrode V_{gt} . Bottom panel: Electrostatic potential profile, $\phi(x = 0, y)$, transverse to the channel (solid red line), with chemical potential ϕ_e (red line), and the distribution of electron density $n_s(y)$ along the y -direction (teal line). (c) Transport measurements performed at various values of V_{gt} , showing the three characteristic transport regimes. Here, $V_{res} = 0.9$ V, $V_{ac} = 20$ mV, $f_{ac} = 1.408$ MHz. For a complete device and transport description, see Section II A and II B.

II. EXPERIMENTAL SETUP

A. Microchannel device for plasmon confinement

Microchannel device architectures, like the one we employ, are widely used to study the effect of geometric confinement on the thermodynamic ground state and transport properties of electrons on helium. Typically in these devices, micron-scale deep channels are filled with superfluid helium via capillary forces and electrons are deposited above the superfluid surface. Metallic electrodes around the channels precisely shape the electrostatic environment to control the spatial distribution of surface state electrons and perform transport experiments [47, 48]. These types of channeled devices have been used to reveal dynamical ordering of two-dimensional [49, 50] and quasi-one-dimensional electron chains [51, 52], and perform ultra-efficient clocking of electrons in microchannel-based CCD arrays [53, 54]. Here we leverage a microchannel architecture to engineer the spatial structure of the two-dimensional electron system in order to host and investigate charge density oscillations, i.e. plasmons.

The device is fabricated on a $7 \text{ mm} \times 2 \text{ mm}$ high resistivity silicon chip, onto which hard-baked resist is deposited and selectively etched to create $h \simeq 1.4 \text{ } \mu\text{m}$ deep channels. As shown in Fig. 1a, four electrodes are lithographically patterned to define two reservoir areas connected via a central microchannel region having a length of $L = 90 \text{ } \mu\text{m}$ and a width of $w = 7 \text{ } \mu\text{m}$. The device is placed into a superfluid-leak-tight sample cell that is mounted onto the mixing chamber plate of a dilution refrigerator. Helium gas from a room temperature volume is introduced into the sample cell, where it condenses into a superfluid and fills the channels via capillary ac-

tion. Electrons are deposited onto the superfluid surface via thermal emission from a tungsten filament.

The high degree of spatial control and confinement over the electrons in the reservoirs and microchannel regions are enabled by voltages (V_i) applied to the four electrodes: V_{gt} (gate), V_{ch} (channel), V_{res} (reservoirs), and the guard electrode. These voltages allow us to control the two-dimensional electrostatic environment experienced by the electrons in the plane of the helium surface $\phi(x, y) = \sum_i V_i \alpha_i(x, y)$ (see Fig. 1b), where the constant $\alpha_i(x, y)$ describes the capacitive coupling between the electrons and the corresponding i^{th} electrode. To design a given confinement profile, we numerically solve the Laplace equation using finite element modelling (FEM) techniques [55]. This allows us to extract α_i and construct the potential by applying appropriate values of V_i . This numerical procedure also allows us to calculate the areal electron density $n_s(x, y)$ for a given potential.

By controlling the electrostatic environment in this fashion, we can effectively create a resonant cavity for confined plasmonic modes, i.e. oscillations of the charge density δn_s , along the length of the central channel. At the boundaries of the microchannel, electrons are free to enter and exit into the reservoir regions, enforcing charge density nodes at the ends of the channel, as depicted in Fig. 1a. Because the number of electron rows is $\gtrsim 10$ in the density regime in which we investigate plasmons, the electrons in the central channel can be modeled as a two-dimensional sheet of charge defined by the electrostatic confinement produced by the electrode voltages. The long and narrow geometry ($L \gg w$) of the central channel ensures a large separation in frequency between plasmons along, versus perpendicular, to the channel. This allows us to consider only longitudinal plasmon standing-waves along the channel length, which have the following dis-

persion relation [34, 56, 57],

$$\omega_p^2 = \frac{n_s e^2}{2\varepsilon_0 m_e} \sqrt{q_x^2 F(q_x)}, \quad (1)$$

where ω_p is the density-dependent frequency of a plasmon having wavevector $q_x = n\pi/L$ and mode number n , m_e is the electron mass, e is the electron charge, and ε_0 is the vacuum permittivity. The wavevector-dependent factor $F(q_x)$ takes into account the reduction in the electron-electron interaction due to the presence of the nearby metallic electrodes. This screening factor will correspondingly reduce the plasmon frequency [34], and for the geometry of our device we utilize the following phenomenological form for $F(q_x)$,

$$F(q_x) = \frac{1}{2}(\tanh q_x l + \tanh q_x h), \quad (2)$$

where $l = w - w_e$ parameterizes the effective distance of the electron sheet from the surrounding side gate electrodes and $h = 1.4 \mu\text{m}$ is the height of the electrons above the bottom channel electrode. The effective width w_e of the electron system is defined where the parabolic confinement potential of the channel is equal to the chemical potential ϕ_e , i.e. $\phi(y = w_e/2) = \phi_e$, as shown in the bottom panel of Fig. 1b, which we extract from FEM. For the specific geometry of our device, which includes laterally defined side gate electrodes, an analytical solution for the screening factor is lacking. However, we find that the phenomenological form presented in Eq. 2 captures to good approximation the screening contributions in the long wavelength limit ($q_x h, q_x l \ll 1$), as well as in the limiting case, in which the screening electrodes are moved infinitely far from the electrons in the channel and the unscreened plasmon dispersion is recovered, i.e. $F(q_x) = 1$. Using Eq. 1 and FEM calculations, we find a fundamental ($n = 1$) plasmon mode frequency of $\omega_p/2\pi \simeq 1.0$ GHz at $n_s \simeq 2.3 \times 10^{12} \text{ m}^{-2}$. This lowest frequency mode corresponds to a half wavelength standing wave of the time-varying change in density δn_s along the channel, as shown in the top panel of Fig. 1a. In the following section, we discuss how these modes are generated using an additional microwave drive, and detected using transport techniques.

B. Transport measurements & microwave excitation

To characterize the electron system in the central microchannel, and its collective dynamics, we utilize a conventional ac transport measurement scheme [51]. In these measurements, an ac voltage V_{ac} is superimposed on the left reservoir electrode driving electrons from one reservoir to the other via the central channel at a frequency f_{ac} . The resulting electron transport through the channel is detected from the voltage V_s induced on the right reservoir electrode, which we measure using standard phase-

sensitive lock-in techniques. As described previously, a dc voltage V_{ch} applied to the channel electrode controls the population of electrons in the central microchannel. In Fig. 1c we show a standard transport map as we tune the electron density and confinement potential in the central channel. This type of measurement reveals three transport regimes depending on the density of electrons in the central microchannel. In regime I, $\phi(y = 0) < \phi_e$, and electrons cannot enter the channel from the reservoirs. When $\phi(y = 0) = \phi_e$ electrons enter the microchannel and form a highly conducting state (regime II) in which the electrons interact weakly with the helium surface, resulting in a large transport signal [49]. At sufficiently high density, the electrons in the microchannel form a low-conductivity Wigner solid (regime III) [58]. These measurements also allow us to calculate the electron density in the central microchannel n_s from the potential in the center of the channel $\phi^0 \equiv \phi(x = 0, y = 0)$ and the chemical potential ϕ_e , as

$$n_s = \frac{\varepsilon_{\text{He}} \varepsilon_0}{eh} (\phi^0 - \phi_e) \quad (3)$$

where, $\varepsilon_{\text{He}} = 1.057$ is the dielectric constant of liquid helium. Here, the chemical potential is calculated using $\phi_e = V_{\text{ch}}^{\text{th}} \alpha_{\text{ch}}^0$ and the capacitive coupling constant in the center of the microchannel, $\alpha_{\text{ch}}^0 \equiv \alpha_{\text{ch}}(x = 0, y = 0) \simeq 0.7$, is obtained through FEM calculations of the device.

To generate plasma oscillations of this electron sheet, we apply a high-frequency signal $\omega/2\pi$ to the gate electrodes located on either side of the microchannel as shown in Fig. 1a. The microwave power modulates the otherwise static confinement potential throughout the microchannel, which leads to a periodic modulation of the effective width w_e of the electron system (see top panel Fig. 1b). The periodic modulation of the potential creates charge density oscillations of the electrons in the central microchannel due to the strong Coulomb interaction. The frequency and amplitude of these oscillations are controlled by the frequency of the gate modulation and the power P of the microwave signal respectively.

III. RESULTS & DISCUSSION

A. Plasmon detection

In Fig. 2, we show how the GHz-frequency plasmonic modes of the electrons in the central microchannel are imparted on the transport signal by monitoring V_s as a function of V_{ch} as we increase the power P of a $\omega/2\pi = 5.5$ GHz signal applied to the gate electrodes. In these measurements, we observe the three characteristic transport regimes described in Sec. II B, corresponding to (I) no electrons, (II) a low-density, highly conducting electron state, and (III) a high-density, low-conductivity Wigner solid within the central channel. With increasing microwave power, the electron density n_s corresponding

to the transition into the low-conductivity Wigner solid increases [59], as shown by the vertical dashed lines for each trace, and we find that this type of effect occurs independent of the frequency of the microwave drive.

More interestingly, with increasing microwave power, we observe the emergence of resonance-like features in the transport signal when the electrons in the microchannel are in the highly conducting state (regime II). Three resonances are clearly visible in the green trace in Fig. 2 at $V_{\text{ch}} = 0.58, 0.68, 0.96$ V corresponding to densities of $n_s = 5.7, 8.6, 16.9 \times 10^{12} \text{ m}^{-2}$ in the central channel. The resonances appear as local minima in the transport signal indicative of a reduction in the conductivity of the electron system in the central channel.

To understand these experimental features, we must consider the non-linear transport phenomena arising from the coupling of the electrons to the helium surface when the system is subjected to the effects of the ac driving and microwave excitation fields, which drive the electrons out of equilibrium [60–62]. We begin by noting that, at $T \simeq 20$ mK, in the absence of microwave excitation and at low ac driving, the electron system would remain in the low-conductivity regime (III) for all values of the electron density shown in Fig. 2. In other words, the *equilibrium* state of the electrons in these experiments corresponds to the low-conductivity Wigner solid [63]. In this regime the electrons coherently emit ripples having wavevectors matching the reciprocal lattice vectors of the electron crystal, a phenomenon known as the resonant Bragg-Cherenkov scattering effect [58]. This effect results in an increased frictional force on the electrons and a saturation of their velocity at the phase velocity of the emitted ripples $v_{\text{ph}} = \omega_r(G_1)/G_1$, where $\omega_r(k) = \sqrt{\sigma_t/\rho} \cdot k^3$ is the ripplon dispersion relation, $\sigma_t = 358 \text{ } \mu\text{N/m}$ is liquid helium surface tension, $\rho = 145 \text{ kg/m}^3$ is the liquid helium density, and $G_1 = (8\pi^2 n_s/\sqrt{3})^{1/2}$ is first reciprocal lattice vector of the Wigner solid. When subjected to high driving fields, the electron system can heat [64], and transition to a non-equilibrium state having a high conductivity (regime II). This state has been interpreted as the formation of either a disordered electron liquid state [65] or as a depinning transition of the Wigner solid [49, 59, 66, 67]. Despite the lack of an unambiguous microscopic description of these nonlinear effects, the transition into the high-conductivity regime (II) strongly depends on the positional order of the electrons in both models. Reducing this order weakens the Bragg-Cherenkov scattering and lowers the critical field required to transition into the high-conductivity state. For the experimental data presented in Fig. 2 transport measurements were performed at driving fields sufficiently high to promote the electrons into the non-equilibrium high-conductivity state for densities $n_s < 18.83 \times 10^{12} \text{ m}^{-2}$.

The additional application of the microwave excitation field onto the side gate electrodes further perturbs the electron system. In the Wigner solid state, these perturbations induce high-frequency electron motion, which in a quasi-static approximation ($\omega \gg \omega_r$) can be viewed

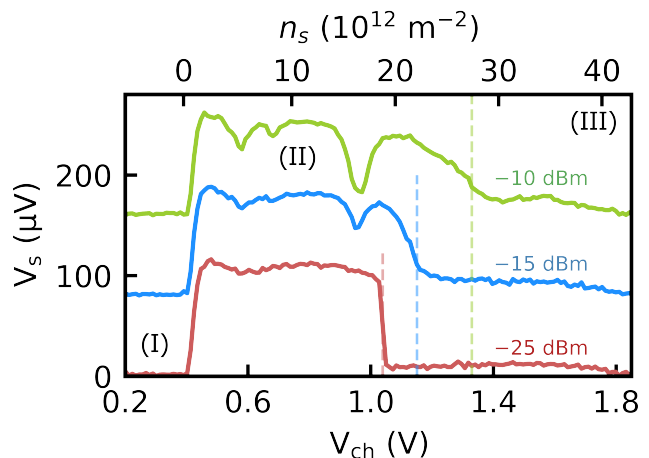


FIG. 2. Microchannel transport measurements in the presence of a $\omega/2\pi = 5.5$ GHz microwave excitation signal on the gate electrode for increasing values of the microwave power P . Traces are offset vertically for clarity and color coded with the corresponding P . Vertical dashed lines indicate the transition into a low-conductivity Wigner crystal electron state, which increases with increasing P . At $P \gtrsim -15$ dBm, resonance-like features appear in regime II, indicating plasmon modes generated along the length of the channel as described in the main text. Measurements performed at $T = 18$ mK, with $V_{\text{ac}} = 6$ mV, $f_{\text{ac}} = 3$ MHz, $V_{\text{res}} = 0.4$ V.

as a weakening of the positional order of the electron solid. As a result, the transition into the low-conductivity Bragg-Cherenkov scattering regime shifts to higher densities with increasing amplitude of the perturbing field. This effect is analogous to raising the temperature of the electron system T_e , which characterizes the melting of the solid. Due to the large electron-electron collision rate (10^{11} s^{-1}) and small energy relaxation rate ($10^5 - 10^6 \text{ s}^{-1}$), the electron system temperature can be raised above that of the helium bath [68]. In this way, the perturbing field effectively melts the Wigner solid leading to a transition into the high-conductivity regime. The ultimate electron temperature produced by the microwave field is determined by a balancing of the incident microwave and drive field powers with the energy transferred into the helium bath via the emission of short-wavelength ripples and phonons. Due to the complex geometry of the device, which includes multiple regions with varying electron density, and the lack of information about the incident microwave power, estimating T_e is unfeasible. Nonetheless, as we discuss below, a qualitative approach can be employed to interpret the decrease in the measured transport signal at the position of the resonances shown in Fig. 2.

Independent of the underlying microscopic state of the electron system in regime II, the microwave energy absorbed by the electrons increases when plasmons are resonantly excited and results in a higher electron temperature on resonance. Since the resonances appear in the high-conductivity regime (II), an increase in T_e can be

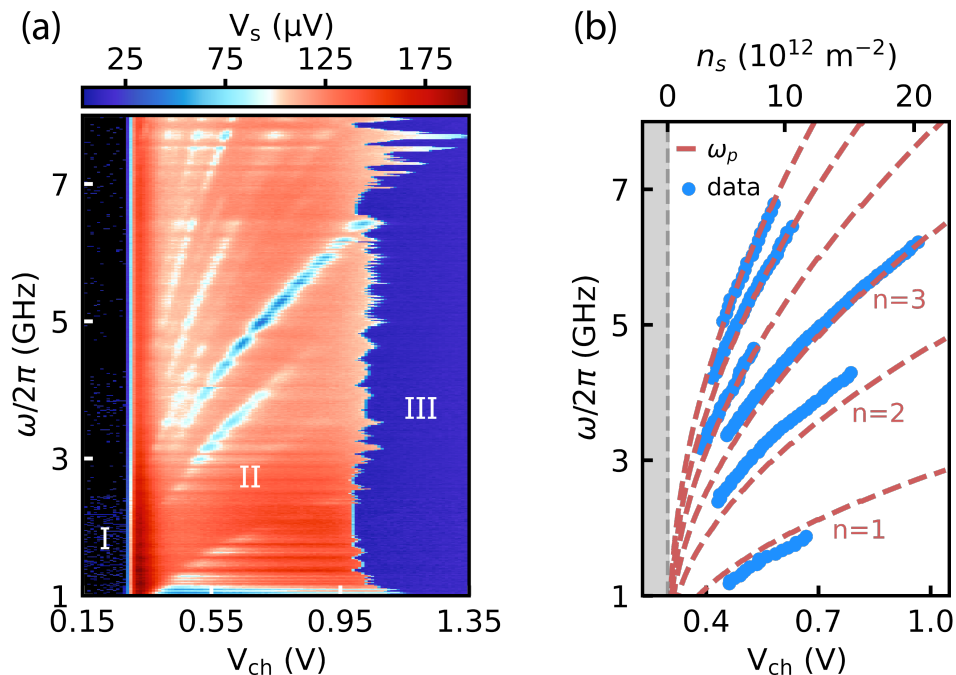


FIG. 3. (a) Microwave frequency dependent transport map. Transport measurements are performed by sweeping V_{ch} to control the electron density in the central channel while simultaneously applying a microwave signal $\omega/2\pi$ to the gate electrodes. For $V_{\text{ch}} \lesssim 0.30$ V, the channel is empty (I). Above $V_{\text{ch}}^{\text{th}}$ electrons can enter the microchannel and form a low-density high-conductivity state (II) and high-density low conductivity Wigner solid (III). The transport signal V_s reveals a family of density and frequency dependent plasmon resonances that manifest as local minima in regime II. Measurements were performed at $P = -15$ dBm, with $V_{\text{ac}} = 8$ mV, $f_{\text{ac}} = 3$ MHz, $V_{\text{res}} = 0.29$ V, and $T = 26$ mK. (b) Blue dots are the extracted local minima from the first six resonances in (a). Red dashed lines correspond to the first six longitudinal plasmon modes along the channel, calculated using the dispersion relation given in Eq. 1 with our device design parameters. Grey shaded region indicates the empty channel (I).

understood as producing an increase in the momentum transfer rate to ripplons, leading to a reduction in the mobility of an electron liquid state [64]. We note that, in principle, the reduction in the measured transport signal on resonance could also be interpreted as a transition from a unpinned Wigner solid into the Bragg-Cherenkov non-linear regime. However, our experiments indicate that in the presence of the microwave excitation, the high-conductivity regime consistently remains in a linear transport regime, indicative of an electron liquid state (see Supplementary Information).

These transport measurements, conducted with an additional perturbing microwave field, reveal the high sensitivity of the measured signal to the presence of plasmonic excitations in the electron system confined within the microchannel. These experiments underscore the complex nature of the non-equilibrium and nonlinear response of this strongly correlated low-dimensional electron system coupled to the helium surface excitations and enrich the extensive body of research on these topics [60, 61, 64, 66, 67, 69]. Despite the absence of an unequivocal microscopic picture of the electron conductivity in these regimes, we can leverage the sensitivity of these measurements to investigate the plasmonic excitations we generate in the central microchannel. Finally we note, a similar technique has recently been employed to

detect the excitation of Rydberg-like resonances of electrons on helium due to resonant microwave heating [62].

B. Analysis of plasmon mode structure

In Fig. 3a we show the full channel density and microwave frequency dependence of the transport signal through the device. In regime II, we observe a family of density-dependent resonances in the channel, which are consistent with the long-wavelength two-dimensional longitudinal plasmons described by Eq. 1. To analyze these plasmon modes, we extract the local transport minima along each of the first six resonances (blue dots in Fig. 3b) and compare them to the calculated values of ω_p using Eq. 1 and our device geometry parameters (red dashed lines). In this calculation, the effective width w_e of the electron system and the corresponding central microchannel electron density n_s are calculated using FEM for each value of V_{ch} . As shown in Fig. 3b, we find excellent agreement between the data and the modeling for the fundamental plasmon mode and its harmonics with no free parameters. The results reveal plasmon modes in a frequency range compatible with cQED systems, and that their frequency can be electrostatically tuned over an extremely broad range ($\approx 2 - 3$ GHz) by controlling

the areal density of electrons.

The data show the resonances appearing only in regime II and not in the low-conductivity Wigner solid (regime III). This is consistent with a significant reduction of the charge density oscillation frequency arising from the phononic modes of the crystal when they are coupled to the elementary excitations of the helium surface (ripplons). In the long wavelength limit, this coupling to ripplons reduces the bare longitudinal plasmon frequency by a factor of $\sqrt{m/m^*}$ [70], where $m^* \gtrsim 100m_e$ parameterizes the effective mass of electrons on helium in the Wigner solid state [71]. Finally, we note the data in Fig. 3b show the transition to the low-conductivity Wigner solid state is significantly non-uniform as a function of microwave drive frequency. This non-resonant effect could be associated with the absorption of microwave energy by other parts of the device, e.g. the resist layer between the top and bottom electrodes or variable microwave transmission due to impedance mismatches in the drive line.

C. Plasmon lineshape & electron density profile

Collective excitations, such as plasmons, are naturally sensitive to the boundary conditions imposed by their environment. In our device, the overall electrostatic potential in the vicinity of the central microchannel controls not only the overall density of electrons in the channel, but also the level of homogeneity in their spatial distribution. The long and narrow aspect ratio of the central channel creates an electron density profile that varies transverse to the length of the channel as shown in Fig. 1b, where we plot the density along the y -direction determined from FEM. In contrast, along the length of the microchannel, the channel electrode produces a relatively homogeneous electron density profile. This spatial inhomogeneity in the electron density will naturally lead to a distribution of plasmons in the channel and a corresponding finite linewidth of the resonances.

To investigate this inhomogeneous broadening we perform transport measurements as a function of microwave power at a fixed frequency $\omega/2\pi = 5.5$ GHz. As shown in Fig. 4a, this microwave drive generates the $n = 7, 5,$ and 3 plasmon modes (from left to right, respectively), which broaden with increasing power. As it is the most prominent, we will focus on the $n = 3$ mode at $V_{\text{ch}} \simeq 0.96$ V for the remainder of this discussion. The experimentally measured composite spectrum, $S(n_s)$, of a given resonance (see Fig. 4) arises from the convolution of the intrinsic lineshape of the mode, $\mathcal{I}(n_s)$, with the density dependent probability distribution of plasmons, $p(n_s)$, which encodes the level of spatial inhomogeneity of the electron density in the channel,

$$S(n_s) = \int \mathcal{I}(n'_s) p(n_s - n'_s) dn'_s. \quad (4)$$

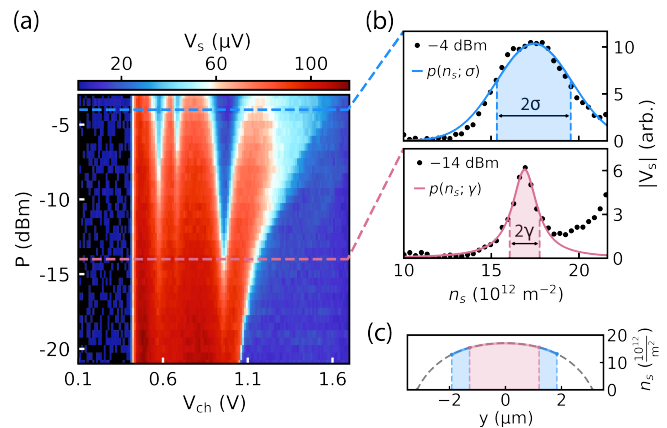


FIG. 4. (a) Microwave power dependent transport measurements at fixed microwave excitation frequency $\omega/2\pi = 5.5$ GHz. With increasing power the resonant plasmon modes broaden significantly. Measurements were performed at $V_{\text{ac}} = 6$ mV, $f_{\text{ac}} = 3$ MHz, $V_{\text{res}} = 0.4$ V, and $T = 18$ mK. (b) Line cuts show the qualitative change in the spectral lineshape of the $n = 3$ plasmon mode at low versus high microwave power. Lines are fit to extract the inhomogeneous plasmon density distribution $p(n_s)$. At low power ($P = -14$ dBm), $p(n_s)$ is well-described by a Lorentzian distribution (pink linecut), while at high power ($P = -4$ dBm), $p(n_s)$ resembles a Gaussian distribution (blue linecut). (c) Electron density across the central channel calculated via FEM. Density distribution at low (pink) and high (blue) power correspond to regions in the center of the microchannel where the plasmons are most strongly generated.

For the value of V_{ch} corresponding to the $n = 3$ mode, FEM analysis indicates that the electron density varies over a large range ($\Delta n_s \simeq 18 \times 10^{12} \text{ m}^{-2}$) transverse to the microchannel (see bottom panel of Fig. 1b), from its highest value in the center of the channel to zero at the edges where the electron sheet terminates. The microwave drive will selectively excite plasmons at a fixed density near the center of the channel, however the Coulomb interaction will generate charge oscillations of the electrons in other regions of channel with different densities and correspondingly different plasma frequencies. If we assume the inhomogeneous density profile in the channel is the dominant mechanism leading to the broadening of $S(n_s)$, the experimentally observed spectrum provides a measure of the probability distribution $p(n_s)$, i.e. $S(n_s) \approx p(n_s)$. We extract this distribution by fitting the spectral lineshapes in Fig. 4a at the different levels of microwave drive power.

At low microwave power we find that the plasmon spectrum is well-described by a Lorentzian lineshape (see pink low power linecut in Fig. 4b). If we ascribe the broadening of this spectrum exclusively to inhomogeneity in the electron density we find that $S(n_s) \approx p(n_s; \gamma) = \frac{\gamma}{\pi(n_s^2 + \gamma^2)}$, where $2\gamma = 1.73 \times 10^{12} \text{ m}^{-2}$ is the full width at half maximum (see pink line cut in Fig. 4) and corresponds to a frequency band of approximately 285 MHz. Comparing

this level of density variation to our FEM calculations indicates that the microwave drive is most strongly generating plasmons in a relatively narrow region of width $\simeq 2.5 \mu\text{m}$ in the center of the channel where the density corresponds to a plasmon of frequency $\simeq 5.5 \text{ GHz}$, as shown in the pink shaded region of Fig. 4c.

At higher power, the fixed frequency drive generates a larger amplitude oscillation of the electrons in the channel, which conspires with the Coulomb interaction to excite charge density waves over a larger region of the channel. As the drive power increases, we find the resonance spectrum inherits a broader, Gaussian-like line-shape, indicating a qualitative change in the distribution of plasmons generated by the drive (see blue high power linecut in Fig. 4b). If we again assume that this broadening is dominated by the electron inhomogeneity in the channel, we find $S(n_s) \approx p(n_s; \sigma) = \frac{e^{-n_s^2/2\sigma^2}}{\sigma\sqrt{2\pi}}$, where $2\sigma = 4.25 \times 10^{12} \text{ m}^{-2}$, corresponding to a frequency band of approximately 690 MHz. At this higher power, the width of the region in which plasmons are most effectively excited in the central channel also increases ($\simeq 3.8 \mu\text{m}$), as shown in the blue shaded region of Fig. 4c.

These results reveal that an increasing microwave drive produces an increase in the spatial extent of the charge density oscillations throughout the channel. This interpretation is also consistent with the observation that the higher order modes ($n = 7$ and $n = 5$), which correspond to a smaller effective width w_e and a smaller electron density variance, have relatively narrower spectral lines.

IV. CONCLUSION

In summary, we have demonstrated a microchannel device architecture that enables us to precisely engineer spatially confined microwave frequency plasmonic modes in electrons on helium. The generation of these plasmons resonantly drives the electron system out of equilibrium, which we detect via low-frequency ac transport measurements of the device conductivity. Precise control over the electrostatic environment of the microchannel confined electrons enables tunability of the plasmons over a frequency range of $\sim 3 \text{ GHz}$ and we find excellent agreement between the observed plasmonic mode structure and the two-dimensional screened plasmon dispersion relation. Power-dependent measurements of the plasmon spectra reveal the interplay between the microwave drive and the intrinsic electron density distribution in the device, which can inform the design of future devices.

The high degree of spatial control and broad microwave frequency tunability provided by this type of microchannel device offers a compelling framework for integrating charged collective oscillations of electrons on helium with circuit quantum electrodynamic systems. Devices utilizing an improved and optimized microwave environment will ultimately be needed for future cQED experiments

with ensembles of electrons on helium. Placing the many-electron on helium system into high-quality factor microwave cavities opens entirely new avenues for exploring cavity optoplasmonics with collective modes in both the Coulomb liquid and solid phases. Similarly, integration with charge sensitive superconducting qubits [72] would enable fast readout of individual and collective electron dynamics and could be used to reveal the microscopic breakdown in the coupling of the electrons to the quantum field of helium surface waves [49, 73]. Alternatively, hybrid systems composed of electrons on helium coupled to superconducting qubits could be used as a model system for understanding qubit decoherence produced by charged fluctuators [74, 75] in a systematic and tunable fashion.

ACKNOWLEDGMENTS

We are grateful to M.I. Dykman, N.O. Birge, J.R. Lane, J.M. Kitzman, G. Koolstra and K. Nasyedkin for valuable discussions. We also thank R. Loloee and D. Edmunds for technical assistance and B. Bi for device fabrication advice and use of the W.M. Keck Microfabrication Facility at MSU. The Michigan State University portion of his work was supported by the National Science Foundation via grant number DMR-2003815 and the Cowen Family Endowment at MSU.

Appendix

To characterize the non-equilibrium transport response of the electron system in the presence of the microwave excitation field, we perform a series of ac drive dependent transport measurements with and without simultaneous microwave power applied to the side gate electrodes. Fig. 5a shows the density dependent transport through the central microchannel with increasing ac drive amplitude and with no microwave excitation on the side gate electrode. At low ac drive ($V_{ac} < 12 \text{ mV}$), the electron system remains in a low-conductivity Wigner solid state for all values of the electron density shown in Fig. 5a. In this regime, the electron velocity saturates at the ripplon velocity as described in Section III A of the main text. At $V_{ac} \simeq 12 \text{ mV}$, the electron system conductivity abruptly increases, indicative of the transition into a high-conductivity state of the electron system, which can be interpreted as either an unpinned Wigner solid or a disordered electron liquid [76].

In Fig. 5b we present a similar ac drive dependent transport measurement but with a $\omega/2\pi = 5.5 \text{ GHz}$ microwave tone applied to the side gate electrode. The presence of the $n = 3$ plasmon mode appears as a reduction in the measured transport signal (solid purple line) as described in Section III A of the main text. Additionally, and in contrast to the case with no microwave excitation (Fig. 5a), the non-linear Bragg-Cherenkov regime is not

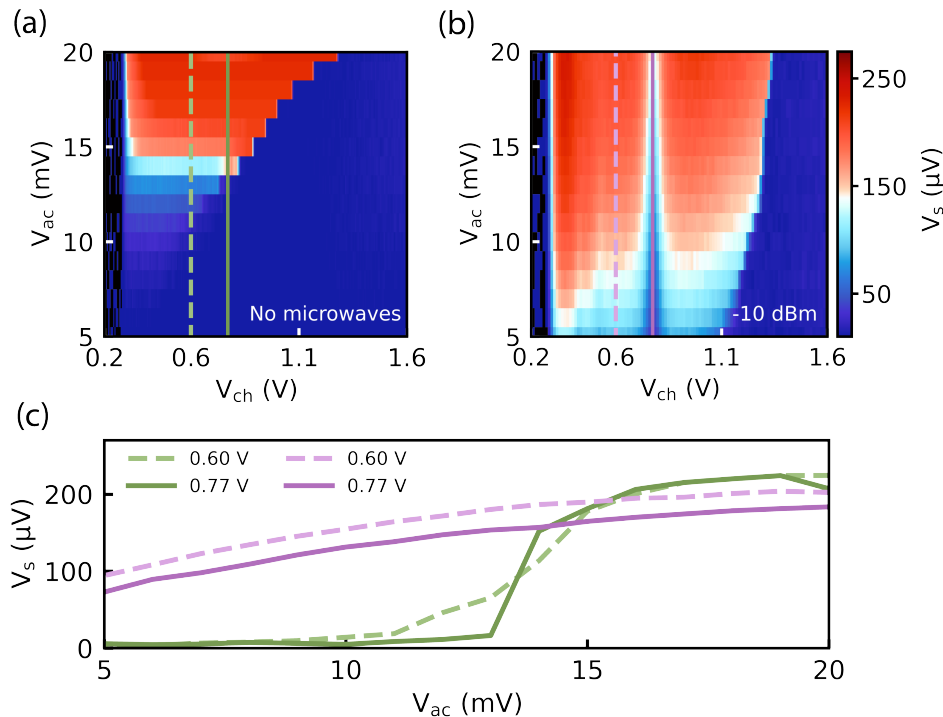


FIG. 5. Drive-dependent transport measurements at $T = 16$ mK with and without microwave side gate excitation. (a) Density-dependent microchannel transport with increasing ac drive voltage, V_{ac} , with no microwave power applied to the side gate electrode. This measurement was performed at $f_{\text{ac}} = 3$ MHz, $V_{\text{res}} = 0.7$ V, and $V_{\text{gt}} = 0$ V. Green dashed ($V_{\text{ch}} = 0.6$ V) and solid ($V_{\text{ch}} = 0.77$ V) lines correspond to the linecuts plotted in (c). (b) Transport measurements similar to those presented in panel a) except with the additional application of a $\omega/2\pi = 5.5$ GHz microwave tone applied to the side gate electrode with $P = -10$ dBm. Purple dashed ($V_{\text{ch}} = 0.6$ V) and solid ($V_{\text{ch}} = 0.77$ V) lines correspond to the linecuts plotted in (c). (c) For additional clarity we show vertical line cuts of the transport signal from panel (a) (green dashed and solid) and panel (b) (purple dashed and solid).

observed down to the lowest levels of ac drive for which we are able to perform transport measurements. Rather we observe steady increase in the transport signal with

increasing ac drive amplitude both on and off resonance (see purple linecuts in Fig. 5c), which is consistent with the heating of an underlying electron liquid state.

-
- [1] A. Wallraff, D. I. Schuster, A. Blais, L. Frunzio, R.-S. Huang, J. Majer, S. Kumar, S. M. Girvin, and R. J. Schoelkopf, *Nature* **431**, 162 (2004).
- [2] A. Blais, A. L. Grimsmo, S. M. Girvin, and A. Wallraff, *Rev. Mod. Phys.* **93**, 025005 (2021).
- [3] M. Aspelmeyer, T. J. Kippenberg, and F. Marquardt, *Rev. Mod. Phys.* **86**, 1391 (2014).
- [4] A. Blais, R.-S. Huang, A. Wallraff, S. M. Girvin, and R. J. Schoelkopf, *Phys. Rev. A* **69**, 062320 (2004).
- [5] K. D. Petersson, L. W. McFaul, M. D. Schroer, M. Jung, J. M. Taylor, A. A. Houck, and J. R. Petta, *Nature* **490**, 380 (2012).
- [6] G. Koolstra, G. Yang, and D. I. Schuster, *Nat. Commun* **10**, 5323 (2019).
- [7] X. Zhou, G. Koolstra, X. Zhang, G. Yang, X. Han, B. Dizdar, X. Li, R. Divan, W. Guo, K. W. Murch, D. I. Schuster, and D. Jin, *Nature* **605**, 46 (2022).
- [8] X. Zhou, X. Li, Q. Chen, G. Koolstra, G. Yang, B. Dizdar, Y. Huang, C. S. Wang, X. Han, X. Zhang, D. I. Schuster, and D. Jin, *Nat. Phys* 10.1038/s41567-023-02247-5 (2023).
- [9] M. LaHaye, J. Suh, P. Echternach, K. C. Schwab, and M. L. Roukes, *Nature* **459**, 960 (2009).
- [10] A. D. O’Connell, M. Hofheinz, M. Ansmann, R. C. Bialczak, M. Lenander, E. Lucero, M. Neeley, D. Sank, H. Wang, M. Weides, J. Wenner, J. M. Martinis, and A. N. Cleland, *Nature* **464**, 697 (2010).
- [11] J. D. Teufel, T. Donner, D. Li, J. W. Harlow, M. Allman, K. Cicak, A. J. Sirois, J. D. Whittaker, K. W. Lehnert, and R. W. Simmonds, *Nature* **475**, 359 (2011).
- [12] J. Pirkkalainen, S. U. Cho, J. Li, G. S. Paraoanu, P. J. Hakonen, and M. A. Sillanpää, *Nature* **494**, 211 (2013).
- [13] A. Clerk, K. Lehnert, P. Bertet, J. Petta, and Y. Nakamura, *Nat. Phys* **16**, 257 (2020).
- [14] M. Goryachev, W. G. Farr, D. L. Creedon, Y. Fan, M. Kostylev, and M. E. Tobar, *Phys. Rev. Appl* **2**, 054002 (2014).
- [15] Y. Tabuchi, S. Ishino, T. Ishikawa, R. Yamazaki, K. Us-

- ami, and Y. Nakamura, Phys. Rev. Lett **113**, 083603 (2014).
- [16] Y. Tabuchi, S. Ishino, A. Noguchi, T. Ishikawa, R. Yamazaki, K. Usami, and Y. Nakamura, Science **349**, 405 (2015).
- [17] J. Li, S.-Y. Zhu, and G. Agarwal, Phys. Rev. Lett **121**, 203601 (2018).
- [18] D. Lachance-Quirion, S. P. Wolski, Y. Tabuchi, S. Kono, K. Usami, and Y. Nakamura, Science **367**, 425 (2020).
- [19] Q. Xu, H. F. H. Cheung, D. S. Cormode, T. O. Puel, S. Pal, H. Yusuf, M. Chilcote, M. E. Flatté, E. Johnston-Halperin, and G. D. Fuchs, Adv. Sci **11**, 2310032 (2024).
- [20] M. V. Gustafsson, T. Aref, A. F. Kockum, M. K. Ekström, G. Johansson, and P. Delsing, Science **346**, 207 (2014).
- [21] Y. Chu, P. Kharel, W. H. Renninger, L. D. Burkhardt, L. Frunzio, P. T. Rakich, and R. J. Schoelkopf, Science **358**, 199 (2017).
- [22] K. J. Satzinger, Y. P. Zhong, H. S. Chang, G. A. Peairs, A. Bienfait, M.-H. Chou, A. Y. Cleland, C. R. Conner, E. Dumur, J. Grebel, I. Gutierrez, B. H. November, R. G. Povey, S. J. Whiteley, D. D. Awschalom, D. I. Schuster, and A. N. Cleland, Nature **563**, 661 (2018).
- [23] M. Bild, M. Fadel, Y. Yang, U. Von Lüpke, P. Martin, A. Bruno, and Y. Chu, Science **380**, 274 (2023).
- [24] J. Kitzman, J. Lane, C. Undershute, P. Harrington, N. Beysengulov, C. Mikolas, K. Murch, and J. Pollanen, Nat. Commun **14**, 3910 (2023).
- [25] J. M. Kitzman, J. R. Lane, C. Undershute, M. Drimmer, A. J. Schleusner, N. R. Beysengulov, C. A. Mikolas, and J. Pollanen, Appl. Phys. Lett **123**, 224001 (2023).
- [26] Y. Kubo, F. R. Ong, P. Bertet, D. Vion, V. Jacques, D. Zheng, A. Dr'ea, J. Roch, A. Auffeves, F. Jelezko, J. Wrachtrup, M. F. Barthe, P. Bergonzo, and D. Esteve, Phys. Rev. Lett. **105**, 140502 (2010).
- [27] D. I. Schuster, A. P. Sears, E. Ginossar, L. DiCarlo, L. Frunzio, J. J. L. Morton, H. Wu, G. A. D. Briggs, B. B. Buckley, D. D. Awschalom, and R. J. Schoelkopf, Phys. Rev. Lett. **105**, 140501 (2010).
- [28] P. Platzman and M. Dykman, Science **284**, 1967 (1999).
- [29] M. Dykman, P. Platzman, and P. Seddighrad, Phys. Rev. B **67**, 155402 (2003).
- [30] M. Dykman, O. Asban, Q. Chen, D. Jin, and S. Lyon, Phys. Rev. B **107**, 035437 (2023).
- [31] S. Lyon, Phys. Rev. A **74**, 052338 (2006).
- [32] N. R. Beysengulov, O. S. Schoyen, S. D. Bilek, J. B. Flaten, O. Leinonen, M. Hjorth-Jensen, J. Pollanen, H. E. Kristiansen, Z. J. Stewart, J. D. Weidman, and A. K. Wilson, PRX Quantum **5**, 030324 (2024).
- [33] D. Schuster, A. Fragner, M. Dykman, S. Lyon, and R. Schoelkopf, Phys. Rev. Lett **105**, 040503 (2010).
- [34] C. Grimes and G. Adams, Phys. Rev. Lett **36**, 145 (1976).
- [35] C. Grimes and G. Adams, Phys. Rev. Lett **42**, 795 (1979).
- [36] D. Mast, A. Dahm, and A. Fetter, Phys. Rev. Lett **54**, 1706 (1985).
- [37] D. C. Glatli, E. Y. Andrei, G. Deville, J. Poitrenaud, and F. I. B. Williams, Phys. Rev. Lett. **54**, 1710 (1985).
- [38] M. J. Lea, P. Fozooni, P. J. Richardson, and A. Blackburn, Phys. Rev. Lett **73**, 1142 (1994).
- [39] A. D. Chepelianskii, D. Papoular, D. Konstantinov, H. Bouchiat, and K. Kono, Phys. Rev. B **103**, 075420 (2021).
- [40] I. Kostylev, M. Hatifi, D. Konstantinov, and A. Chepelianskii, arXiv preprint arXiv:2404.07582 (2024).
- [41] K. M. Yunusova, D. Konstantinov, H. Bouchiat, and A. Chepelianskii, Phys. Rev. Lett **122**, 176802 (2019).
- [42] A. Zadorozhko, J. Chen, A. Chepelianskii, and D. Konstantinov, Phys. Rev. B **103**, 054507 (2021).
- [43] H. Byeon, K. Nasyedkin, J. R. Lane, N. R. Beysengulov, L. Zhang, R. Loloee, and J. Pollanen, Nat. Commun **12**, 4150 (2021).
- [44] L. Abdurakhimov, R. Yamashiro, A. Badrutdinov, and D. Konstantinov, Phys. Rev. Lett **117**, 056803 (2016).
- [45] J. Chen, A. Zadorozhko, and D. Konstantinov, Phys. Rev. B **98**, 235418 (2018).
- [46] G. Yang, A. Fragner, G. Koolstra, L. Ocola, D. Czaplewski, R. Schoelkopf, and D. Schuster, Phys. Rev. X **6**, 011031 (2016).
- [47] D. Marty, J. Phys. Condens. Matter **19**, 6097 (1986).
- [48] D. G. Rees, I. Kuroda, C. A. Marrache-Kikuchi, M. Höfer, P. Leiderer, and K. Kono, Phys. Rev. Lett **106**, 026803 (2011).
- [49] D. G. Rees, N. R. Beysengulov, J.-J. Lin, and K. Kono, Phys. Rev. Lett **116**, 206801 (2016).
- [50] S. Zou, D. Konstantinov, and D. G. Rees, Phys. Rev. B **104**, 045427 (2021).
- [51] P. Glasson, V. Dotsenko, P. Fozooni, M. Lea, W. Bailey, G. Papageorgiou, S. Andresen, and A. Kristensen, Phys. Rev. Lett **87**, 176802 (2001).
- [52] D. G. Rees, N. R. Beysengulov, Y. Teranishi, C.-S. Tsao, S.-S. Yeh, S.-P. Chiu, Y.-H. Lin, D. A. Tayurskii, J.-J. Lin, and K. Kono, Phys. Rev. B **94**, 045139 (2016).
- [53] G. Sabouret, F. Bradbury, S. Shankar, J. Bert, and S. Lyon, Appl. Phys. Lett **92** (2008).
- [54] F. Bradbury, M. Takita, T. Gurrieri, K. Wilkel, K. Eng, M. Carroll, and S. A. Lyon, Phys. Rev. Lett **107**, 266803 (2011).
- [55] N. Beysengulov, D. Rees, Y. Lysogorskiy, N. Galiullin, A. Vazjukov, D. Tayurskii, and K. Kono, J. Low Temp. Phys **182**, 28 (2016).
- [56] Y. Monarkha and K. Kono, *Two-Dimensional Coulomb Liquids and Solids*, 1st ed., Springer Series in Solid-State Sciences (Springer Berlin, Heidelberg, 2004).
- [57] E. Y. Andrei, ed., *Two-Dimensional Electron Systems*, 1st ed., Physics and Chemistry of Materials with Low-Dimensional Structures (Springer Dordrecht, 1997).
- [58] M. Dykman and Y. G. Rubo, Phys. Rev. Lett **78**, 4813 (1997).
- [59] D. G. Rees, S.-S. Yeh, B.-C. Lee, S. K. Schnyder, F. I. Williams, J.-J. Lin, and K. Kono, Phys. Rev. B **102**, 075439 (2020).
- [60] D. Konstantinov, H. Isshiki, H. Akimoto, K. Shirahama, Y. Monarkha, and K. Kono, J. Phys. Soc. Jpn **77**, 034705 (2008).
- [61] K. Nasyedkin, V. Syvokon, and Y. Monarkha, J. Low Temp. Phys **163**, 148 (2011).
- [62] S. Zou, S. Grossenbach, and D. Konstantinov, J. Low Temp. Phys **208**, 211 (2022).
- [63] In this regime the electron system is in equilibrium with the helium bath, thus for an electron temperature $T_e = 20$ mK the critical density to form a Wigner Solid ($n_s^{cr} = 8 \times 10^9 \text{ m}^{-2}$) is reached for $(V_{ch} - V_{ch}^{th}) > 0.2$ mV.
- [64] M. Saitoh, J. Phys. Soc. Jpn **42**, 201 (1977).
- [65] M. Dykman, personal communication (2024).
- [66] K. Shirahama and K. Kono, Phys. Rev. Lett **74**, 781 (1995).
- [67] H. Ikegami, H. Akimoto, and K. Kono, Phys. Rev. Lett **102**, 046807 (2009).

- [68] D. Glatli, E. Andrei, and F. Williams, *Phys. Rev. Lett* **60**, 420 (1988).
- [69] Y. P. Monarkha and V. E. Syvokon, *Low Temp. Phys* **38**, 1067 (2012).
- [70] D. S. Fisher, B. Halperin, and P. Platzman, *Phys. Rev. Lett* **42**, 798 (1979).
- [71] M. A. Stan and A. J. Dahm, *Phys. Rev. B* **40**, 8995 (1989).
- [72] K. Serniak, S. Diamond, M. Hays, V. Fatemi, S. Shankar, L. Frunzio, R. Schoelkopf, and M. Devoret, *Phys. Rev. A* **12**, 014052 (2019).
- [73] M. I. Dykman, *Physics* **9**, 54 (2016).
- [74] J. M. Martinis, K. B. Cooper, R. McDermott, M. Steffen, M. Ansmann, K. D. Osborn, K. Cicak, S. Oh, D. P. Pappas, R. W. Simmonds, and C. C. Yu, *Phys. Rev. Lett.* **95**, 210503 (2005).
- [75] P. V. Klimov, J. Kelly, Z. Chen, M. Neeley, A. Megrant, B. Burkett, R. Barends, K. Arya, B. Chiaro, Y. Chen, A. Dunsworth, A. Fowler, B. Foxen, C. Gidney, M. Giustina, R. Graff, T. Huang, E. Jeffrey, E. Lucero, J. Y. Mutus, O. Naaman, C. Neill, C. Quintana, P. Roushan, D. Sank, A. Vainsencher, J. Wenner, T. C. White, S. Boixo, R. Babbush, V. N. Smelyanskiy, H. Neven, and J. M. Martinis, *Phys. Rev. Lett.* **121**, 090502 (2018).
- [76] M. Dykman, *Physics* **9** (2016).